Materials Research Bulletin 143 (2021) 111450

Contents lists available at ScienceDirect

Materials Research Bulletin

journal homepage: www.elsevier.com/locate/matresbu

Research Papers

Large enhancement of thermal conductance at ambient and cryogenic temperatures by laser remelting of plasma-sprayed Al_2O_3 coatings on Cu

Álvaro Cubero [a], Elena Martínez [a,*], Germán F. de la Fuente [a], Irene García Cano [b], Sergi Dosta [b], Luis A. Angurel [a]

[a] Instituto de Nanociencia y Materiales de Aragón (INMA), CSIC-Universidad de Zaragoza, Zaragoza 50009, Spain
[b] Centre de Projecció Tèrmica (CPT), Dept. Ciència de Materials i Química Física, Universitat de Barcelona, Barcelona, Spain

ARTICLE INFO

Keywords:
Laser melting
Plasma-sprayed coatings
Thermal contact conductance
Heat sink
Cryogenic temperatures

ABSTRACT

Joints of high thermal contact conductance and electrical insulation have been obtained by coating copper supports with thin alumina (Al_2O_3) layers (of 140–150 μm thickness). This has been achieved by a combination of plasma spraying process and the subsequent coating remelting by a near-Infrared (n-IR) laser. With a proper optimization of the laser processing conditions, it is possible to transform the metastable γ-Al_2O_3 phase of the as-sprayed coatings to stable α-Al_2O_3, and to achieve denser alumina coatings. This results in a large enhancement of the thermal conductance of the joints, enabling their application as heat sinks at cryogenic and ambient temperatures. The process proposed in this work is scalable for the formation of alumina coatings on large metallic pieces of complex geometries.

1. Introduction

Many power applications require the use of heat sinks to adequately transfer the heat generated in the system to the cold focus, thus avoiding excessive temperature rise and the eventual damage of the device. The development of technological applications based on MgB_2 and high temperature superconductors using cryocoolers allows operating temperatures between 20 K and 77 K (boiling temperature of liquid nitrogen at atmospheric pressure). In these superconducting devices, such as magnets and the current leads feeding them, heat intercept connections working from room temperature down to the operating cryogenic temperatures are particularly crucial for those systems cooled by conduction and working under high vacuum [1–3].

For demountable joints, heat transfer across the solid-solid interface is the main component of the overall thermal resistance. Thus, the needed optimization of bolted joints implies the achievement of low thermal boundary resistances. This is strongly determined by the thermal and physical properties of the contact material surfaces, such as geometry, roughness and topography, as well as the type of materials in the interface (metal-metal, metal-ceramic, etc.), their bulk thermal conductivity, κ, and the interposition of intermediate layers (usually, Apiezon-N grease or indium foil for cryogenic applications) [1,4,5]. The thermal contact resistances of mechanical contacts between two solids of different materials have been studied at temperatures close and above room temperature and also below 4.2 K [1,4,5,6], but there are few results at intermediate temperatures, between 20 K and 300 K [7].

The metallic materials in the heat sink should be electrically insulated from those carrying current. Alumina single crystal, sapphire, has been widely used with this aim in cryogenic applications due to its high thermal conductivity at low temperatures (2900 $Wm^{-1}K^{-1}$ at 10 K) [1]. However, the use of single crystals is limited to small elements, with typical contact areas of around 1 cm^2. When larger contact areas are needed, low temperature epoxy resins and fiberglass-epoxy composites have been used [8–10], but their thermal conductivities are usually much lower, typically < 1 $Wm^{-1}K^{-1}$ below 77 K [1]. In contrast, some sintered ceramics such as Al_2O_3, AlN and BN [11], exhibit high thermal conductivity at ambient and cryogenic temperatures, with increasing values for denser ceramics with low impurity concentration [1,12]. However, their main drawback arises from the difficulty of machining and obtaining complex-shaped parts [13]. Besides, the differences in thermal contraction of the dissimilar materials that form the heat sink cause thermal stress during cooling down to cryogenic temperatures. This can result in a drastic decrease of the thermal conductance of the joint and also produce large cracks in the ceramic material [14]. The use of large size bulk ceramics is thus normally disregarded for this cryogenic application.

* Corresponding author.
E-mail address: elenamar@unizar.es (E. Martínez).

https://doi.org/10.1016/j.materresbull.2021.111450
Received 26 February 2021; Received in revised form 7 June 2021; Accepted 20 June 2021
Available online 24 June 2021

Thermal sprayed coatings on metals, which are widely used as a barrier to protect the metal component from abrasive or corrosive environments or high heat conditions, can also provide additional functionalities [15,16]. The use of plasma-sprayed alumina coatings on a metallic substrate to achieve the dual function of providing electrical insulation together with a good thermal conductance was first proposed by Mackay and Muller [17] for heat sinks in electronic packaging at ambient temperatures. This technology may solve the above-mentioned problems of bulk ceramics, as it can be used to fabricate parts with no limitations in size and with very diverse shapes. The copper or aluminum substrates can be easily machined to the desired geometry for the application, including the holes for bolt joints, before plasma spraying of the ceramic coated layer. One main drawback of as-sprayed coatings is their high porosity, which would result in lower thermal conductivity as compared to corresponding high density pure ceramics. Moreover, the presence of the metastable phases gives rise to some undesired effects, as it can produce a deterioration of the dielectrical properties of alumina [18].

Laser remelting of the plasma-sprayed Al_2O_3 coatings can overcome this problem, by achieving a denser and more homogenous layer. CO_2-laser melting of ceramic coatings (such as alumina or alumina-based eutectics) on pure metals or alloys has been reported by several groups [19–28], mainly with the aim of enhancing their mechanical properties. CO_2 lasers are frequently used due to the much higher absorption values measured at λ= 10.6 μm in comparison with those obtained at λ ≈1 μm [29,30]. The advantage of using mid-IR CO_2 lasers is obvious, as 10.6 μm radiation absorption is nearly at the 90% level in Al_2O_3, while it is only about 3% under 1 μm irradiation at an irradiance level of 10^4 Wcm^{-2} [29]. Although other ceramic materials, like those based on ZrO_2, enable increased absorption at ca. 1 μm laser wavelengths, apparently because of the presence of defects associated to oxygen vacancies [30], Al_2O_3 behaves quite differently. Its absorption at λ≈1 μm may be more significant when in powder form, because of the presence of pores [31] and difficult to control in a sustained manner when highly densified [31,32]. The use of pulsed ns lasers enables improved melt stability control [31] and has thus paved the way towards increased use of near-infrared (n-IR) lasers [30,33,34]. Some cracks in the ceramic layer can be produced during this process due to thermal shock caused by the rapid heating and cooling processes intrinsic to laser heating [34–36]. One alternative to reduce thermal stresses is to induce a preheating step using two lasers, for instance, a larger spot CO_2 laser for heating the sample and a smaller spot n-IR laser within the preheated large spot to melt the ceramic surface [37]. A more industrially scalable alternative is to perform the laser treatment when the sample is moving at constant speed inside a furnace at high temperature [38]. Laser processing conditions should be then carefully analyzed to overcome this unwanted effect, with the aim of minimizing the number, size and impact of microcracks in the final sample properties.

This work aimed at enhancing thermal contact resistance of plasma-sprayed Al_2O_3 coatings on copper for their use in cryogenic and ambient temperature applications, by subsequently remelting of the ceramic layer using n-IR laser irradiation at room temperature. Laser processing parameters have been found to affect strongly the microscopic properties of the final coating. Optimized processing conditions are thus a key issue to minimize the presence of cracks and obtain a final dense ceramic layer. The thermal contact resistance of representative samples processed under optimized conditions is herein reported and compared with the behavior of non-irradiated samples.

2. Experimental and methods

2.1. Plasma spraying of Al_2O_3 coatings on copper

Alumina coatings were produced by atmospheric plasma spraying (APS). APS coatings were sprayed on copper substrates using the F4 gun attached to an A3000S system (automated and robotized) from Sulzer Metco, with argon and hydrogen employed as process gasses. The applied parameters of 600A intensity, 35/12 Ar/H_2 l/min gas flow and 120 mm distance were selected based on previous knowledge, as given in references [39–41].

The surface of the copper substrate was subjected to a grit blasting process before coating. Commercial Al_2O_3 powders of 10 to 20 μm particle size, provided by H.C. Starck were used. The alumina coating thickness was set around 150 μm and its surface had typical roughness Ra values of 5 - 7 μm (measured in representative areas of 600 μm x 400 μm). Copper of 99.9% purity, residual-resistance ratio, RRR = 80, with 5 mm thickness and area of 1 cm × 2 cm was used as substrate.

2.2. Laser processing

Al_2O_3 coatings were irradiated with a n-IR Ytterbium pulsed fiber laser (Perfect Laser, model PEDB-400B), with central wavelength λ = 1060–1070 nm, $1/e^2$ beam diameter $2r_b$ = 65 μm, using a pulse repetition frequency, f_{rep} = 900 kHz, and pulse duration τ_p = 200 ns. Given a nominal average laser power, P_L, each laser pulse is characterized by its energy, E_p ($E_p = P_L/f_{rep}$), its fluence, F_p ($F_p = E_p/(\pi r_b^2)$) and its irradiance, I_p ($I_p = F_p/\tau_p$). Laser processing was carried out using the meandering laser beam scanning (MLBS) method, where the laser beam follows a meander-shaped path in order to completely irradiate the whole substrate sample surface (see Fig. 1). Each scanned line starts and ends outside the sample. The combination of pulse fluence, laser beam scanning velocity (v_L) and hatch distance between adjacent lines (d_s), determines the total accumulated fluence, which takes into account the overlap between consecutive pulses in a line and between adjacent lines:

$$F_{2D} = \frac{\pi\, r_b^2}{d_p\, d_s}\, F_p \tag{1}$$

Here, $d_p = v_L/f_{rep}$ is the distance between the centers of two consecutive laser pulses in a line. The ratios d_p/r_b and d_s/r_b control the degree of overlap in both directions. Table 1 collects some representative laser processing conditions analyzed in this work.

2.3. Microscopy characterization

The microstructure of plasma sprayed coatings, before and after laser processing, was studied by field-emission scanning electron microscopy (FE-SEM), (MERLIN, Carl Zeiss). In general, an accelerating voltage of 3 - 5 kV was used for surface images and 15 kV for cross-sectional views. Different detectors were used: secondary electrons (SE), angle-selective

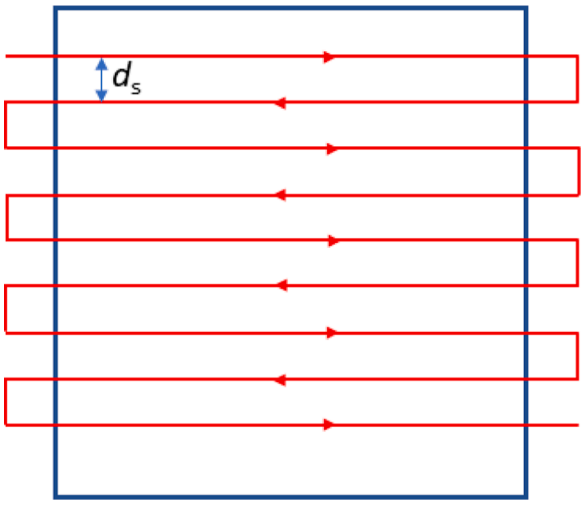

Fig. 1. Scheme of the trajectory of the center of the laser beam in a meandering laser beam scanning (MLBS) configuration.

Table 1
Some representative laser processing parameters used to irradiate the alumina coating.

Name	P_L(W)	v_L(mm/s)	d_s(μm)	d_p(μm)	F_p(J/cm^2)	I_p(MW/cm^2)	F_{2D}(kJ/cm^2)
LP1	27.3	80	15	0.09	0.91	4.57	2.3
LP2	27.3	80	20	0.09	0.91	4.57	1.7
LP3	27.3	80	25	0.09	0.91	4.57	1.4
LP4	27.3	80	30	0.09	0.91	4.57	1.1
LP5	27.3	100	20	0.11	0.91	4.57	1.4
LP6	27.3	50	20	0.055	0.91	4.57	2.7
LP7	31.5	80	20	0.09	1.06	5.27	2.0
LP8	35.0	80	20	0.09	1.17	5.86	2.2

backscattered electrons (AsB) and Inlens. The latter is a high-efficiency annular SE detector used to map the surface structure. The roughness of the coatings was measured by confocal microscopy (sensofar Plμ−200). The phase composition was analyzed by X-ray diffraction (XRD) patterns collected at room temperature on a RIGAKU D-max /2500 X-ray diffractometer using Cu Kα radiation. The "JCPDS-International centre for Diffraction Data- 2000" database was used for phase determination. Rietveld analysis of XRD patterns, using the PDXL 2 commercial software from RIGAKU, was performed to calculate the weight ratio content of the different phases present in the as-sprayed coating.

2.4. Method for characterization of the joint thermal resistance

To determine experimentally the thermal resistance of these joints at cryogenic temperatures, steady-state measurements [42] were performed with the set-up shown in Fig. 2. The analyzed samples were placed between two larger copper plates, which constitute the heat source and heat sink, and are joined between them by two screws. The screws were tightened leaving a space between both copper plates at the edges slightly (≈0.25 mm) lower than the thickness of the sample. The surface contact pressure for this configuration was measured using pressure indicating sensor films (Prescale® from Fujifilm). Note that these films were not used during thermal measurements. Apiezon-N grease was applied over all contact surfaces (ceramic and copper) for thermal measurements.

The heat sink copper plate is mechanically and thermally attached to the cold finger of a cryocooler. It is equipped with a thermometer (T_{cold}) and a heater (HT) that allows controlling the operating temperature of the joint by using a Lakeshore temperature controller. The second copper plate also holds a thermometer (T_{hot}) and another heater HS (heat source), which provides a prefixed constant power, P_0 that can be varied. Heat transfer across the joint takes place mainly by conduction. The convective component is residual as the sample is inside a cryostat in high vacuum ($\approx 10^{-5}$ hPa), and the radiation contribution has also been neglected because of the presence of a thermal radiation shield around the joint. The validity of this hypothesis will be discussed in Section 3.3.

For each measurement run, once the whole joint is at the set temperature, a constant heat power P_0 is applied by the HS, which produces a constant heat flow rate across the joint ($\dot{Q} = P_0$). Eventually, after a time that depends on the enthalpy and the thermal resistance of the joint at this temperature, the system reaches thermal equilibrium, and a

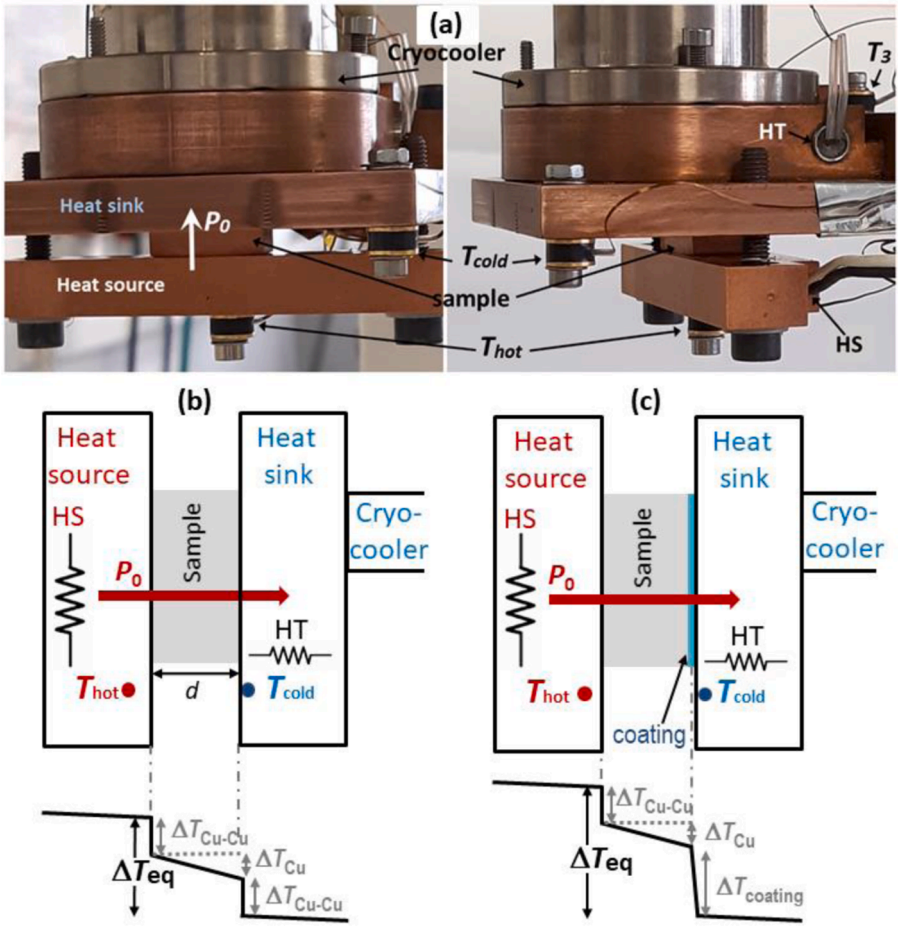

Fig. 2. (a) Photographs of the set-up used for the measurement of thermal contact resistances at cryogenic temperatures (taken at two different angles). (b)-(c) Schematics of set-up and thermal profiles for: (b) reference copper sample; (c) copper coated with alumina. P_0 is the constant heat flow rate across the joint. The cryocooler, heater HT and a temperature controller allows controlling the temperature T_{cold}.

constant temperature difference between T_{hot} and T_{cold} is established, ΔT_{eq}, which is proportional to the overall thermal resistance of the joint at this temperature:

$$R_H(T) \sim \frac{\Delta T_{eq}}{P_0}[\mathrm{K/W}] \quad (2)$$

It should be noted that the temperature difference measured between T_{cold} and T_3 (also placed in the heat sink but further away from the sample) is negligible compared to ΔT_{eq}. Thus, it indicates that the exact location of T_{cold} and T_{hot} (both installed near the sample) is not critical. This is expected because of the high thermal conductivity of the copper and the much larger cross-sectional area for heat flow through the sinks, compared to the sample. The measured R_H (or ΔT_{eq}) value across the joint at each temperature is the sum of different contributions. In the case of the non-coated copper (reference) sample (see Fig. 2b), it is given by the sum of the thermal resistance of the bulk copper and the contact resistance at the two Cu-Cu surfaces, i.e.:

$$R_{H,ref}(T) = R_{H,Cu}(T) + 2R_{H,Cu-Cu}(T) \sim \left(\frac{1}{P_0}\right)(\Delta T_{Cu} + 2\Delta T_{Cu-Cu}) \quad (3)$$

$\Delta T_{\mathrm{Cu\text{-}Cu}}$ is the temperature difference between both copper surfaces in contact. Note that there are two nominally identical Cu-Cu contact surfaces, thus, we assume that similar temperature gradients are generated at both interfaces. ΔT_{Cu} is the temperature drop across the bulk copper sample, given by the thermal conductivity of the used copper, $\kappa_{Cu}(T)$, which is known, its thickness, $d = 5 \times 10^{-3}$ m, and the contact area $A = 2 \times 10^{-4}$ m^2:

$$\Delta T_{Cu} \sim P_0 R_{H,Cu} \text{ with } R_{H,Cu}(T) \sim \frac{1}{\kappa_{Cu}(T)}\frac{d}{A} \quad (4)$$

Thus, using Eqs. (2)–(4), it is possible to estimate the thermal contact resistance between the copper surfaces as:

$$R_{H,Cu-Cu}(T) \sim \frac{\Delta T_{Cu-Cu}}{P_0} \sim \frac{1}{2}\left(R_{H,ref}(T) - R_{H,Cu}(T)\right) \quad (5)$$

In the case of the copper sample with alumina coating on one of their faces (see Fig. 2c), the total resistance across the joint R_H is given by:

$$R_H(T) = R_{H,Cu-Cu}(T) + R_{H,Cu}(T) + R_{H,coating}(T) \sim \left(\frac{1}{P_0}\right)\left(\Delta T_{Cu-Cu} + \Delta T_{Cu} + \Delta T_{coating}\right) \quad (6)$$

Here, the term $R_{H,coating}$ has in turn three contributions: the thermal resistance of the interface between the copper substrate and the alumina coating ($R_{H,subst\text{-}alumina}$), the "bulk" thermal resistance of the alumina layer ($R_{H,alumina}$) and the contact resistance between the surfaces of the alumina and the copper heat sink ($R_{H,alumina\text{-}Cu}$):

$$R_{H,coating}(T) = \frac{\Delta T_{coating}}{P_0} = R_{H,subst-alumina}(T) + R_{H,alumina}(T) + R_{H,alumina-Cu}(T) \quad (7)$$

Although our experimental configuration does not allow measuring separately each term of Eq. (7), it is possible to estimate the overall contribution of the alumina coating ($R_{H,coating}$) to the contact resistance of the joint. According to Eq. (6), this value was obtained from the experimentally measured R_H, the contact resistance $R_{H,Cu\text{-}Cu}$, which was previously derived from the measurement of the non-coated reference sample; and $R_{H,Cu}$, which is given by Eq. (4). The corresponding "equivalent" thermal contact conductance of the coating $h_{j,coating}$, which is normalized to the contact area of the joint, is given by:

$$h_{j,coating}(T) \sim \frac{1}{A}\frac{1}{R_{H,coating}(T)} = \frac{1}{A}\frac{P_o}{\Delta T_{coating}}\left[\mathrm{Wm^{-2}K^{-1}}\right] \quad (8)$$

Before cooling down, the thermal resistance of the joints was also measured at room temperature, 290 K, with the sample in vacuum.

3. Results and discussion

3.1. Microstructure of the laser remelted coatings

Fig. 3 shows SEM micrographs of the surface (Fig. 3a) and cross-sections (Fig. 3b and 3c) of the alumina plasma sprayed coating on copper. The typical features of plasma-sprayed coatings are observed, which are inherent to this technique, where a large number of melted and partially-melted particles is deposited, giving rise to the observed microstructure and surface roughness [18]. The transversal cross-sections of polished samples show the boundary between the alumina coating and the copper substrate (light color in Fig. 3b). As observed in this figure, the alumina layer follows the surface topography of the copper substrate and is highly porous (black areas in the figure). A detail of the coating can be seen in Fig. 3c, showing the lamella stacking structure of the as-sprayed coating, and pores that range typically from 1 μm to 10 μm.

In order to find the optimum MLBS parameters, preliminary studies were carried out by irradiating the surface at different scanning velocities and laser power values, finding a range between 50 and 100 mm/s at P_L higher than 25 W, where this is generally achieved. Thus, a more detailed analysis of laser processing parameter influence was performed by changing systematically one parameter at the time. For this purpose, areas of about 10 mm × 2 mm of an alumina coated copper sample were laser treated under different conditions.

The hatch distance was varied from 5 to 30 μm while fixing $P_L = 27.3$ W and $v_L = 80$ mm/s. Fig. 4 shows the SEM images of four representative sample surfaces, which correspond to d_s of 15, 20, 25 and 30 μm. It was found that the d_s value strongly affects the surface homogeneity of the processed samples. For $d_s = 15$ μm (Fig. 4a), an uneven and irregular surface topography is obtained, with the presence of marked peaks and valleys. These irregularities are even more pronounced when decreasing the hatch distance below 15 μm (not shown). The best results are obtained for $d_s = 20$ μm (Fig. 4b and 4e), which corresponds to $d_s/r_b = 0.615$. Fig. 4e shows a detail of this surface, where elongated grains of alumina aligned parallel to the laser beam scan direction are observed, along with some cracks in the perpendicular direction. A reduced number of micropores are also observed throughout the sample, usually located along the transversal cracks. Surface topography obtained for $d_s = 25$ μm (Fig. 4c) is similar, although with more cracks and pores. By increasing the hatch distance further to 30 μm (Fig. 4d and 4f), the melted surface becomes less uniform, with an increasing size and number of pores and cracks. This result indicates that a certain overlap between adjacent laser scan lines is required, with an optimum condition for $d_s/r_b \sim 0.6$ - 0.7. Note that in those cases the surface becomes smoother than in as-sprayed samples. The Ra measured in representative areas of 600 μm × 400 μm is about 4 μm.

Next, on the basis of the best optimum laser processing conditions obtained in Fig. 4b, the effect of varying the scan velocity and the laser power was analyzed. For this purpose, samples were processed with fixed $d_s = 20$ μm and $P_L = 27.3$ W, varying the laser beam scan velocity between 50 mm/s and 100 mm/s. Fig. 5a and 5b show the surface topography of the samples processed with $v_L = 100$ mm/s and 50 mm/s, respectively. It is observed that the former condition results in very irregular melting, identified by the presence of numerous bumps and holes. It must be remarked here that, even with increasing P_L values, satisfactory results were not achieved using this v_L. On the contrary, by decreasing v_L, the surface appears more homogeneous, although some cracks in the direction perpendicular to the beam scan are still observed (see Fig. 5e). The samples processed with $v_L = 80$ mm/s and increasing power values are shown in Fig. 5c and 5d, respectively. Very homogeneous surfaces were obtained in both cases, with the direction of laser scans clearly visible. Alumina crystals are larger than with the previous processing parameters, as observed in Fig. 5e, and cracks in the perpendicular direction to the beam scan extend longer than in the previously analyzed cases, as larger grains would facilitate the crack

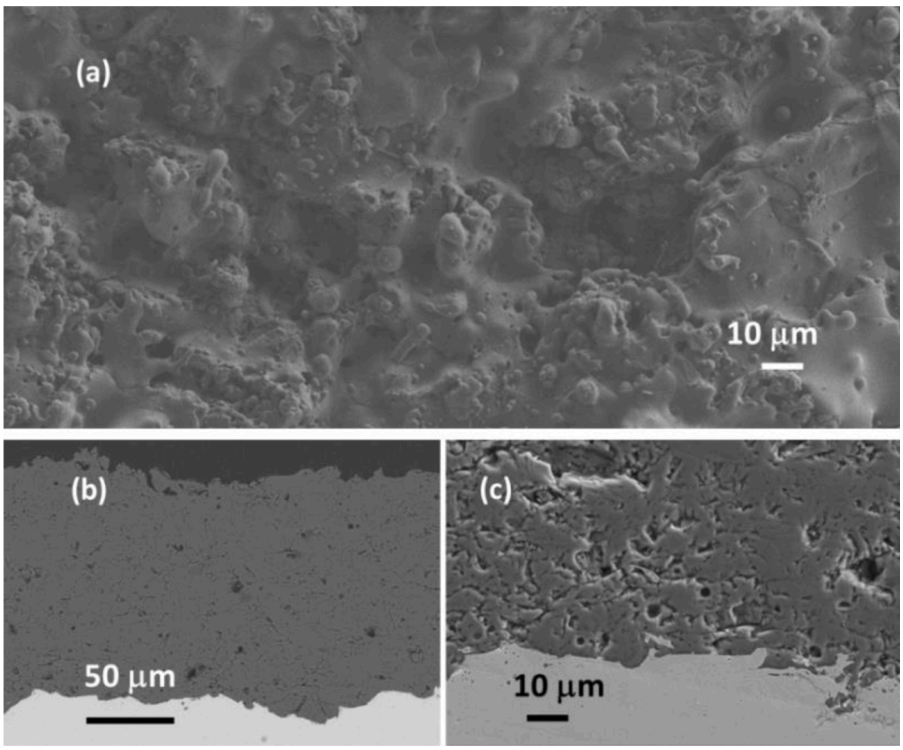

Fig. 3. SEM images of alumina coated samples (as-sprayed), showing (a) the surface topography (SE); (b) and (c) are images of transversal cross-sections of polished samples with different magnifications and detectors: (b) AsB and (c) SE.

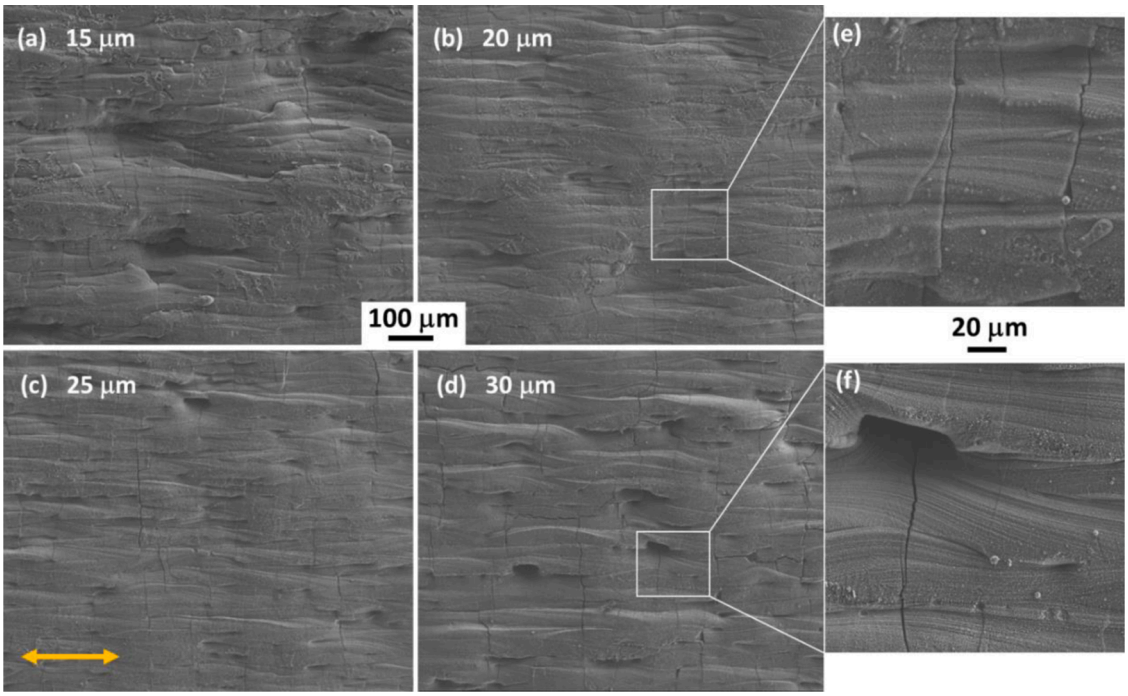

Fig. 4. SEM images (SE) of alumina surfaces processed with the same $P_L = 27.3$ W and $v_L = 80$ mm/s values, and with different hatch values from 15 μm to 30 μm as indicated: (a) LP1, (b) LP2, (c) LP3, (d) LP4. The same magnification was used in the four cases under an applied voltage of 3 kV. (e) and (f) show the areas highlighted by a white rectangle in the corresponding (b) and (d) images, respectively, with higher magnification. The arrow in (c) marks the laser beam scan direction, which is the same for all micrographs.

propagation in this direction.

The observed transverse cracks, i.e., perpendicular to the laser scanning direction, have similar characteristics as those reported by Zheng et al. [34] for Al_2O_3 ceramics obtained by selective laser melting (SLM). These have been attributed to the extremely high temperature gradient and to the internal stress caused by the thermal shock effect of laser reheating. Longitudinal cracks, which have also been observed in alumina SLM specimens, also appear in our study for conditions where

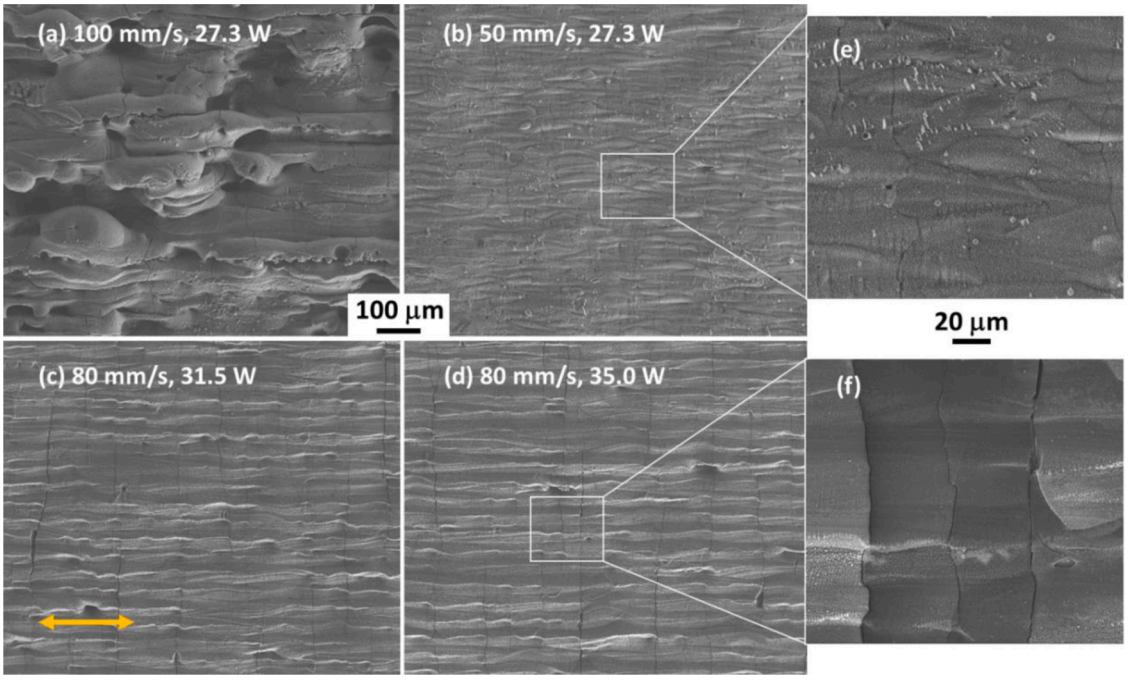

Fig. 5. SEM images (SE) of surfaces processed with a fixed hatch value, $d_s = 20$ µm, obtained with fixed $P_L = 27.3$ W and varying the scanning velocity: (a) LP5, (b) LP6. With fixed v_L and varying P_L: (c) LP7, (d) LP8. The same magnification was used in the four images. (e) and (f) show the areas highlighted by a white rectangle in the corresponding (b) and (d) images, respectively, with higher magnification (in-lens detector). A voltage of 5 kV was used in all images. The arrow in (c) marks the laser beam scan direction, which is the same for all micrographs.

unmelted zones coexist with partially melted ones (see for example Figs. 4a, 4d and 5a), but are scarce in samples with uniformly melted surfaces (LP2, LP6, LP7 and LP8, for example). When laser melting is very inhomogeneous (as the case shown in Fig. 5a), besides the two types of cracks, holes appear abundantly.

The transversal cross-sections of some of the above samples are shown in Fig. 6. In general, all laser processing conditions that give inhomogeneous surface topographies also result in irregular cross-sectional views. For example, laser conditions LP1 (shown in Fig. 6a, corresponding surface in Fig. 4a) produces a columnar-type microstructure, with cracks in the direction perpendicular to the coating-metal boundary. These extend along the entire thickness of the

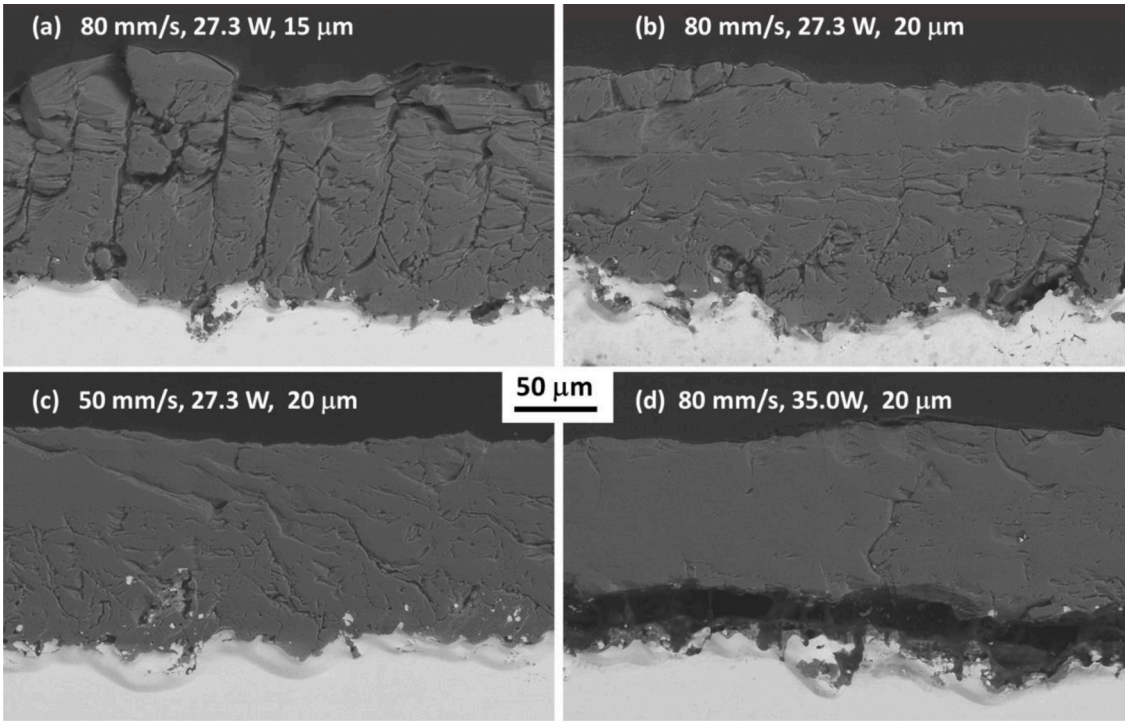

Fig. 6. SEM images (backscattered electrons) of transversal cross-sections of polished samples treated with different laser processing parameters: (a) LP1; (b) LP2; (c) LP6; (d) LP8. The laser beam scan direction is in the direction perpendicular to the plane of the images.

coating. Additionally, cracks in the direction parallel to the surface are also observed near the surface. The corresponding cross-sections of the optimum surface microstructure, LP2 and LP6, previously shown in Figs. 4b and 5b, are shown in Fig. 6b and 6c, respectively. Both are characterized by a layer of dense recrystallized alumina in the upper part of the coating, near the surface, with a more porous layer near the copper. Some holes at the alumina/copper boundary, of about 20 - 30 μm size, are observed. Particles of copper and copper oxide are present in the latter layer, especially in case of LP6. Finally, Fig. 6d shows an example of a fully remelted coating, characterized by the presence of a very dense and homogeneous alumina layer, although this is completely separated from the copper substrate. It is expected that heating of the metallic substrate during laser processing could help to avoid this unwanted effect. For this reason, samples LP2 and LP6 were selected to analyze their thermal behavior, and to compare with as-sprayed samples.

3.2. Phase composition

Fig. 7 shows the X-ray diffraction patterns of two alumina coated samples, in the cases of as-sprayed (a) and after subsequent laser remelting using optimized conditions (LP2) (b). In the former, the main phase corresponds to the metastable γ-Al_2O_3 phase, with the presence of some α-Al_2O_3 (corundum), β-Al_2O_3 and copper (substrate). The weight ratio content of crystalline α-Al_2O_3 and γ-Al_2O_3 phases in the as-sprayed coating was estimated to be 5.8(3)% and 91.3(19)%, respectively. The formation of metastable phases in plasma-sprayed alumina coatings has already been reported [18,43–45] and explained in terms of classical nucleation theory and the thermal history of the particles during solidification [43,46]. After laser remelting under optimum conditions, only the phase corresponding to corundum is essentially present, with a marginal content of the γ-alumina phase (see Fig. 7b).

3.3. Thermal conductance characterization

Thermal contact conductance behavior as a function of temperature was characterized in four representative samples, detailed as follows. A non-coated Cu sample was measured as a reference, as explained in 2.4 (Fig. 2b). Three alumina-coated Cu samples were also measured (Fig. 2c): one of them corresponding to the as-sprayed plasma coating, and the other two were subsequently processed with laser parameter conditions LP2 and LP6. Hereafter, these samples will be referred to as non-coated, as-sprayed, LP2 and LP6, respectively. Each sample was measured twice in order to estimate the error and to check the reproducibility of the measurements. For that purpose, each sample was cooled down and measured at different temperatures. Afterwards, it was warmed up at room temperature, un-installed and installed again, and cooled down for another complete test run. In all cases the differences between two different runs were within 5–8%, without exhibiting any degradation in the second measurement.

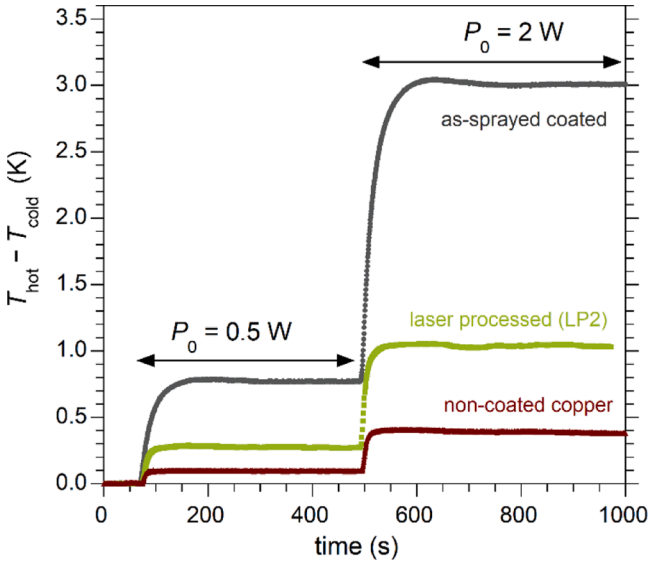

Fig. 8. Temporal evolution of difference between $\Delta T(t) = T_{hot}(t) - T_{cold}(t)$ temperatures across the joint (see Fig. 2) for constant heat flow P_0 = 0.5 W and 2 W at set temperature 50 K. The results correspond to the non-coated Cu, as-sprayed alumina, and laser processed sample with conditions LP2, as indicated.

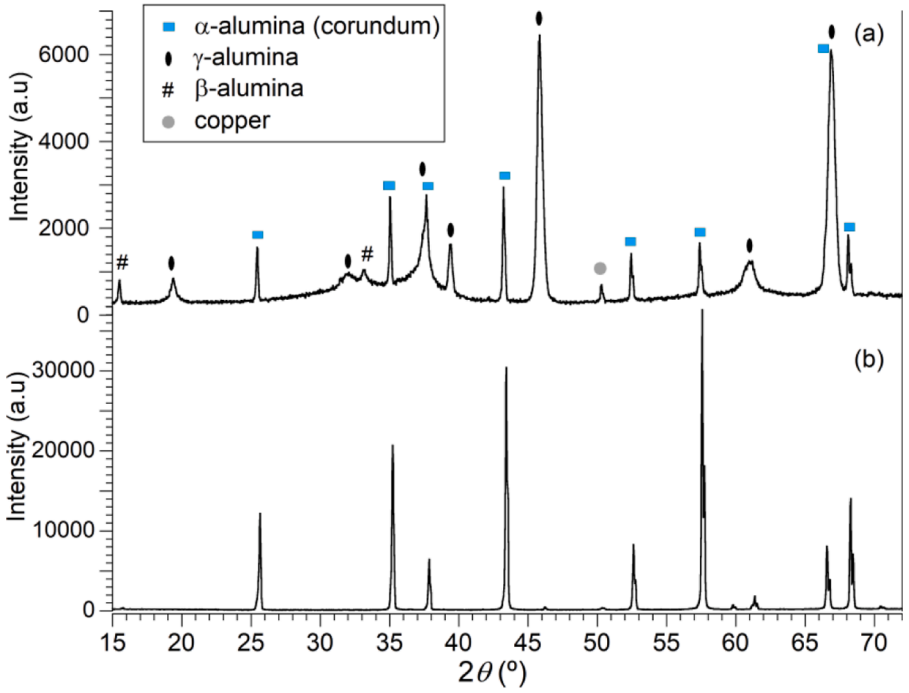

Fig. 7. XRD patterns of alumina coated samples obtained on (a) as-sprayed sample, and (b) on the sample after laser remelting with condition LP2.

Fig. 8 shows the time evolution of the difference between the hot and cold temperatures across the joint, $T_{hot}(t) - T_{cold}(t)$, at a temperature of 50 K, for three different samples: non-coated copper, as-sprayed and laser processed (LP2). In all cases, after setting the constant heat flow, the system reached eventually a steady state and a constant ΔT_{eq} was established for each P_0, which allows the estimation of R_H of the whole joint using Eq. (2). A significant enhancement of the thermal joint is observed for the laser-processed alumina-coated sample, as compared to the as-sprayed coated sample, with a significant reduction of ΔT_{eq} from 3.01 K to 1.03 K, respectively, for $P_0 = 2$ W. The value obtained under similar conditions for the non-coated copper sample was 0.38 K. To calculate the R_H value of the joint at each temperature, different values of P_0 were applied. The results corresponding to sample LP2, for the two different measurements runs and at different temperatures, are plotted in Fig. 9. A good linear fit of the data is obtained, suggesting that the radiation heat income does not vary significantly during each measurement [7], thus supporting the above-mentioned hypothesis.

The temperature dependence of thus derived R_H values is plotted in Fig. 10 for the four analyzed samples. Note that thermal resistance of the bulk copper ($R_{H,Cu}$), which was calculated by Eq. (4) and is also plotted for comparison purposes, does not contribute significantly to the total R_H, as expected. The improved thermal behavior observed for the coated samples with subsequent laser remelting was observed for all measured conditions, from cryogenic to ambient temperatures. The difference becomes particularly marked in the range between 40 K and 77 K, where the R_H values of the laser treated samples are about three times lower than those corresponding to the as-sprayed sample. The larger improvement in this temperature range is due to the temperature dependence of thermal conductivity of α-Al_2O_3, which presents a maximum at this temperature range [1]. An increase of the thermal conductivity of the components of the thermal joint, also results in an improvement of the thermal contact conductance [7].

Fig. 11 displays the values of the corresponding "equivalent" thermal contact conductance of the coating $h_{j,coating}$ (see Eqs. (7) and (8)). These were calculated from $R_H(T)$ curves using the procedure described in Section 2.4. These values include the contribution of the alumina coating layer, as well as the thermal contact resistance between the alumina and the (Cu) heat-sink and at the interface between the (Cu) substrate and the alumina, as explained above. Values of about 0.95×10^4 and 1.55×10^4 $Wm^{-2}K^{-1}$ are obtained for the laser processed sample LP2 at temperatures of 40 K and 77 K, respectively. This is an important enhancement when comparing with as-sprayed coatings or other technologies. For example, Datskov et al. [2] reported heat transfer coefficient of about 3600 $Wm^{-2}K^{-1}$ at 77 K for a heat sink, which consisted in two copper plates with three layers of fiberglass tape between them and were used in conduction-cooled current leads working at a maximum current of 250 A. In previous work [3], our group reported values of about 1800 $Wm^{-2}K^{-1}$ at 80 K for a heat sink made with plasma-sprayed alumina coating on aluminum, for a similar application.

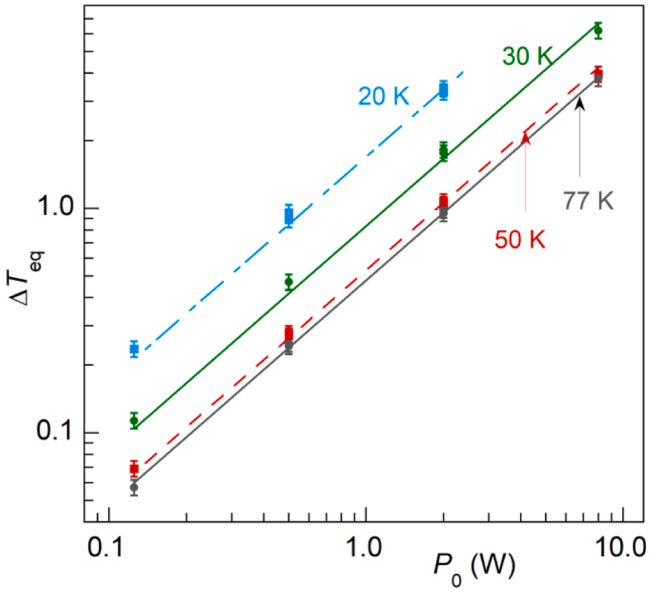

Fig. 9. Measured ΔT_{eq} values (symbols) for sample LP2 as a function of the applied P_0 and at different temperatures. Lines are best fits to Eq. (2).

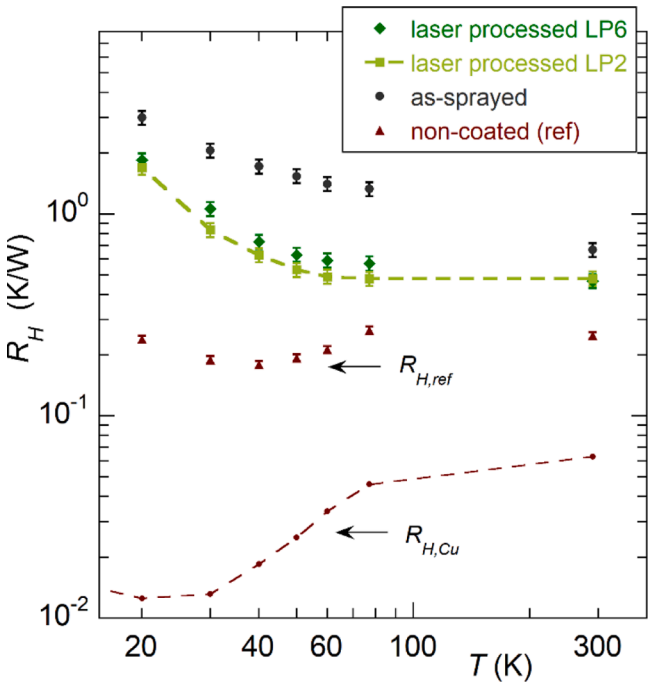

Fig. 10. Temperature dependence of the thermal resistance of the whole joint, R_H, estimated from Eq. (2) for the four measured samples (contact area $A = 2$ cm^2). The contribution of $R_{H,Cu}$ (Eq. (4)) is also plotted for comparison.

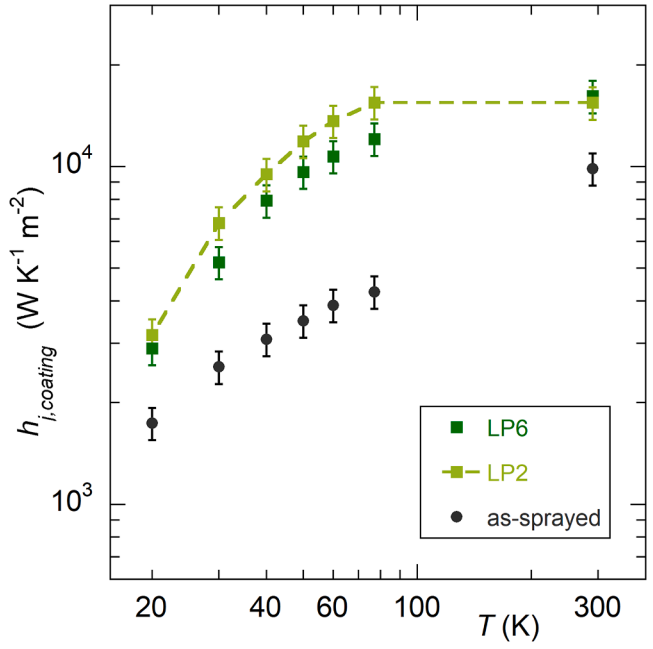

Fig. 11. Temperature dependence of the thermal contact conductance of the coating $h_{j,coating}$ (Eqs. (7) and (8)), for the as-sprayed alumina coatings and laser processed coatings with laser processing conditions LP2 and LP6.

The latter value was estimated from the numerically calculated total heat inleak into the heat sink and the measured ΔT across the whole joint. The obtained results in the present work by laser-processing of the plasma-sprayed coating imply thus a remarkable upgrade, which would allow higher current application (in case of current-leads) and an important improvement of the thermal stability of the system in all cases.

The contact pressure applied during the above thermal measurements was analyzed using pressure indicator films, which were placed at the interface between the heat sink and the coating surface of the sample. Fig. 12 shows the results obtained for three different samples (non-coated, as-sprayed, and laser-processed LP6). For each measurement, which was performed at temperatures of 20–23 °C and relative humidity of 40–50%, the joint was tightened slowly and kept for two minutes, following the manufacturer's instructions [47]. Two different pressure-range films, LW (2.5–10 MPa) and MS (10–50 MPa), were used subsequently for each sample. The density of magenta color corresponds to the applied pressure level, according to the standard chart given by the sensor manufacturer [47]. Fig. 12a shows the results for the reference sample, where the observed color-density saturation in the case of LW sensor indicates that the applied pressure is higher than 10 MPa in the whole contact area. MS-films display higher color densities (≈0.7, corresponding to ≈28 MPa) at the upper and lower parts of the images than at the center, which would be due to the used set-up geometry. The larger roughness of alumina coated samples, both as-sprayed (Fig. 12b) and laser-processed (Fig. 12c), produces a more inhomogeneous pressure distribution, as expected. Some flatness deviations are also observed in both samples. Maximum pressure values are localized at small areas surrounded by others with lower contact pressures. The distribution of these regions clearly reflects the differences in the surface topography between both coated samples. These results would indicate that a further increase of $h_{j,coating}$ could be achieved by decreasing the surface roughness and the flatness-deviation of these samples. Given the surface roughness and contact area characteristics of as-sprayed and laser-processed coatings, the presence of apiezon-N at the interface would be preferable to "dry" contacts in these coated samples [1].

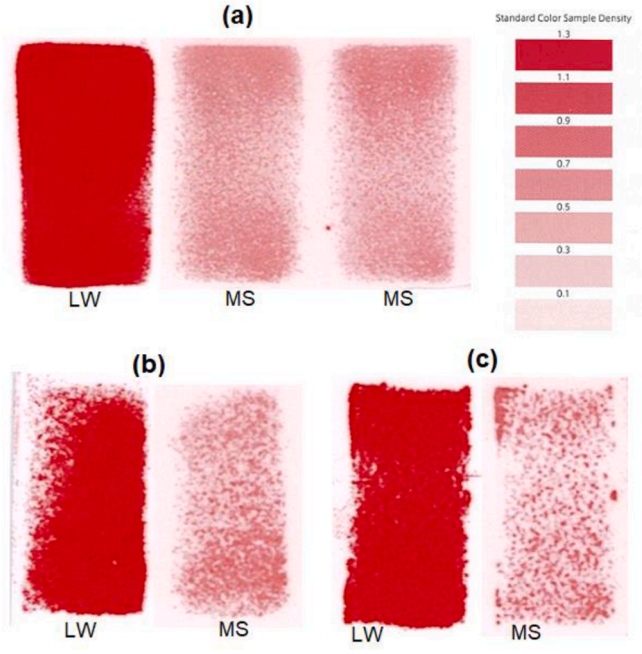

Fig. 12. Pressure-film images using either LW (2.5–10 MPa) or MS (10–50 MPa) sensors, as indicated, for different samples: (a) non-coated Cu sample (two nominally identical MS tests are shown for comparison); (b) as-sprayed alumina coating on Cu; (c) Laser-processed-alumina coating on Cu (LP6). The films were placed between the coating surface and the copper heat sink.

No appreciable damage was observed in the analyzed samples during thermal resistance measurements, despite the different linear contraction from room temperature to cryogenic temperatures of substrate and coating ($\Delta L/L = (L_{293K}–L_T)/L_{293K} = 0.30\%$ and 0.08%, for copper and alumina, respectively, at $T = 77$ K) [1,12]. To further investigate the effect of thermal cycling, laser-processed samples were subjected to an additional number (10) of fast thermal cycling tests, without observing coating failure. For each cycle, the sample was cooled down from room temperature to 77 K by rapid immersion into liquid nitrogen, followed by a 1-minute at 77 K and a 4-minute warm-up at room temperature. It should be reminded here that both copper and alumina undergo little thermal contraction below this temperature [1,12], which is the common behavior of most materials.

It should also be highlighted that the $h_{j,coating}$ values for both analyzed laser-processed samples (LP2 and LP6), which were selected on the basis of their better microstructural characteristics, do not differ significantly. Particularly, the LP2 sample shows slightly higher $h_{j,coating}$ values than LP6, but with differences just above the estimated errors. The fact that both samples exhibit similar thermal behavior indicates that the range of laser parameters resulting in an enhancement of thermal behavior is not narrow. This provides important advantages from a practical point of view. Moreover, this may also indicate that the small differences between both samples would be likely due to the exact number of defects in the final samples. This suggests that a way to achieve further enhancement of these joints could involve heating the substrate (or the whole sample) during laser processing to minimize thermomechanical stress between the molten pool and the recrystallized grains. By doing so, it is expected that the number of cracks and other defects could be further minimized. The purpose would be to achieve denser coating layers (as seen in Fig. 6d), without a degradation of the bonding between the metal and ceramic components. This procedure, however, could have the risk of introducing metallic copper into the alumina layer, which could result in the loss (or deterioration) of its dielectric properties and should be avoided. This would thus require a complete and careful study to probe its viability for this application.

4. Conclusions

Laser remelting of plasma-sprayed alumina coatings on copper have been performed aiming at achieving electrical insulation together with a good thermal conductance. Laser processing was carried out with a meandering laser beam scanning method, using a n-IR Ytterbium pulsed fiber laser, emitting at a central wavelength $\lambda = 1060–1070$ nm, $1/e^2$ beam diameter $2r_b = 65$ μm, pulse repetition frequency of 900 kHz, and pulse duration of 200 ns. The effect of the main laser processing parameters, including pulse fluence (F_p), laser beam scanning velocity (v_L) and hatch distance between adjacent lines (d_s) has been reported. The optimum microstructures were obtained for $F_p \sim 0.9$ J/cm^2, $d_s \sim 20$ μm (corresponding to $d_s/r_b \sim 0.6$) and v_L between 50 and 80 mm/s.

Thermal contact resistance of Cu/Cu-coated demountable joints as a function of temperature was characterized for two laser-processed samples, which were selected on the basis of their better microstructural characteristics. These were composed by a layer of dense recrystallized alumina in the upper part of the coating, near the surface, and a more porous layer near the copper interface. An important improvement of the thermal behavior was observed for these laser treated samples under all conditions, from cryogenic to ambient temperatures, as compared to the as-sprayed samples. The observed differences became particularly marked in the range between 40 K and 77 K, where the thermal resistance R_H values of the laser treated samples were about three times lower than those corresponding to the plasma-sprayed samples. Values of the "equivalent" thermal contact conductance of the coating $h_{j,coating}$ as high as 0.95×10^4 and 1.55×10^4 Wm^{-2}K^{-1} at temperatures of 40 K and 77 K, respectively, were obtained for the

optimized laser processed sample. These values include the contribution of the thermal resistances of the alumina/copper and alumina/substrate interfaces and across the alumina coating layer itself. Further improvement of thermal contact conductance is expected to be possible by simultaneous heating of the substrate or the whole sample during the laser remelting process. This could further minimize the inherent defects in the alumina coating appearing by thermal shock during the rapid melting and cooling associated to laser remelting.

Declaration of Competing Interest

The authors declare that they have no known competing financial interests or personal relationships that could have appeared to influence the work reported in this paper

Acknowledgments

This work was funded by project ENE2017–83669-C4–1-R (MCIU/AEI/FEDER, EU), by the Gobierno de Aragón "Construyendo Europa desde Aragón" (research group T54_20R) and Generalitat de Catalunya for the project SGR2017_01777. The authors acknowledge the use of Servicio General de Apoyo a la Investigación-SAI at the University of Zaragoza.

References

[1] J.W. Ekin, Experimental Techniques For Low-Temperature Measurements, Oxford University Press, 2006.
[2] V. Datskov, A. Bleile, E. Fischer, G. Hess, Conduction-cooled HTS current leads for the SIS100 corrector magnets, IEEE T. Appl. Supercond. 28 (2018), 4801803, https://doi.org/10.1109/TASC.2018.2806946.
[3] A. Cubero, A.B. Núñez-Chico, R. Navarro, L.A. Angurel, E. Martínez, Electromagnetic behaviour and thermal stability of a conduction-cooled, no-insulated 2G-HTS coil at intermediate temperatures, Cryogenics (Guildf) 108 (2020), 103070, https://doi.org/10.1016/j.cryogenics.2020.103070.
[4] A.L. Woodcraft, Comment on 'thermal boundary resistance of mechanical contacts between solids at sub-ambient temperatures, J. Phys. D 34 (2001) 2932–2934, https://doi.org/10.1088/0022-3727/34/18/401.
[5] E.T. Swartz, R.O. Pohl, Thermal boundary resistance, Rev. Mod. Phys. 61 (1989) 605–668, https://doi.org/10.1103/RevModPhys.61.605.
[6] L.J. Salerno, P. Kittle, A.L. Spivak, Thermal conductance of pressed metallic contacts augmented with indium Foil or Apiezon-NTM grease at liquid helium temperatures, NASA Tech. Mem. (1993), 108779JulyAvailable online, https://ntrs.nasa.gov/api/citations/19940009554/downloads/19940009554.pdf.
[7] E. Gmelin, M. Asen-Palmer, M. Reuther, R. Villar, Thermal boundary resistance of mechanical contacts between solids at sub-ambient temperatures, J. Phys. D 32 (1999) R19–R43, https://doi.org/10.1088/0022-3727/32/6/004.
[8] R.C. Niemann, J.D. Gonczy, P.E. Phelan, T.H. Nicol, Design and performance of low-thermal resistance, high-electrical-isolation heat intercept connections, Cryogenics (Guildf) 35 (1995) 829–832, https://doi.org/10.1016/0011-2275(95)90926-7.
[9] J. Pelegrín, G. Romano, E. Martínez, L.A. Angurel, R. Navarro, C. Ferdeghini, S. Brisigotti, G. Grasso, D. Nardelli, Experimental and numerical analysis of quench propagation on MgB_2 tapes and pancake coils, Supercond. Sci. Technol. 26 (2013), 045002, https://doi.org/10.1088/0953-2048/26/4/045002.
[10] S.-.H. Jeong, J.-.B. Song, K.L. Kim, Y.H. Choi, H. Lee, Enhanced thermal properties of epoxy composite containing cubic and hexagonal boron nitride fillers for superconducting magnet applications, Compos. B Eng. 107 (2016) 22–28, https://doi.org/10.1016/j.compositesb.2016.09.066.
[11] G.A. Slack, Nonmetallic crystals with high thermal conductivity, J. Phys. Chem. Solids 34 (1973) 321–335, https://doi.org/10.1016/0022-3697(73)90092-9.
[12] N.J. Simon, Cryogenic Properties of Inorganic Insulation Materials for ITER Magnets, NISTIR 94-5030, National Institute of Standards and Technology, Boulder, CO, 1994. Available online, https://nvlpubs.nist.gov/nistpubs/Legacy/IR/nistir5030.pdf.
[13] M. Qin, H. Lu, H. Wu, Q. He, C. Liu, X. Mu, Y. Wanga, B. Jia, X. Qu, Powder injection molding of complex-shaped aluminium nitride ceramic with high thermal conductivity, J. Eur. Ceram. Soc. 39 (2019) 952–956, https://doi.org/10.1016/j.jeurceramsoc.2018.11.037.
[14] K. Takahata, H. Tamura, T. Mito, S. Imagawa, A. Sagara, A cooling concept for indirectly cooled superconducting magnet for the fusion reactor FFHR, Plasma Fusion Res. 10 (2015), 3405011, https://doi.org/10.1585/pfr.10.3405011.
[15] S. Sampath, Thermal spray applications in electronics and sensors: past, present, and future, J. Therm. Spray Technol. 19 (2010) 921–949, https://doi.org/10.1007/s11666-010-9475-2.
[16] D. Tejero-Martin, M. Rezvani Rad, A. McDonald, T. Hussain, Beyond traditional coatings: a review on thermal-sprayed functional and smart coatings, J. Therm. Spray Technol. 28 (2019) 598–644, https://doi.org/10.1007/s11666-019-00857-1.
[17] T.L. Mackay, A.N. Muller, Plasma-sprayed dielectric coatings for heat sinks in electronic packaging, Am. Ceram. Soc. Bull. 46 (1967) 833.
[18] F.-.L. Toma, L.-.M. Berger, S. Scheitz, S. Langner, C. Rödel, A. Potthoff, V. Sauchuk, M. Kusnezoff, Comparison of the microstructural characteristics and electrical properties of thermally sprayed Al_2O_3 coatings from aqueous suspensions and feedstock powders, J. Therm. Spray Technol. 21 (2012) 480–488, https://doi.org/10.1007/s11666-012-9761-2.
[19] N.R. Quick "Laser processed coatings on electronic circuit substrates" US patent 5,391,841 (1995).
[20] R. Sivakumar, B.L. Mordike, Laser melting of plasma sprayed ceramic coatings, Surf. Eng. 4 (1988) 127–140, https://doi.org/10.1051/jphyscol:1987721.
[21] Y. Yuanzheng, Z. Youlan, L. Zhengyi, Ch. Yuzhi, Laser remelting of plasma sprayed Al_2O_3 ceramic coatings and subsequent wear resistance, Mater. Sci. Eng. A 291 (2000) 168–172, https://doi.org/10.1016/S0921-5093(00)00983-7.
[22] C. Batista, A. Portinha, R.M. Ribeiro, V. Teixeira, M.F. Costa, C.R. Oliveira, Morphological and microstructural characterization of laser-glazed plasma-sprayed thermal barrier coatings, Surf. Coatings Technol. 200 (2006) 2929–2937, https://doi.org/10.1016/j.surfcoat.2004.10.134.
[23] Y. Wang, C.G. Li, W. Tian, Y. Yang, Laser surface remelting of plasma sprayed nanostructured Al_2O_3–13wt%TiO_2 coatings on titanium alloy, Appl. Surf. Sci. 255 (2009) 8603–8610, https://doi.org/10.1016/j.apsusc.2009.06.033.
[24] Y. Wang, C. Li, L. Guo, W. Tian, Laser remelting of plasma sprayed nanostructured Al_2O_3–TiO_2 coatings at different laser power, Surf. Coatings Technol. 204 (2010) 3559–3566, https://doi.org/10.1016/j.surfcoat.2010.04.028.
[25] J. Yu, Y. Wang, F. Zhou, L. Wang, Z. Pan, Laser remelting of plasma-sprayed nanostructured Al_2O_3–20 wt.% ZrO_2 coatings onto 316 L stainless steel, Appl. Surf. Sci. 431 (2018) 112–121, https://doi.org/10.1016/j.apsusc.2017.06.204.
[26] R. Krishnan, S. Dash, R.K. Sole, A.K. Tyagi, B. Raj, Fabrication and characterisation of laser surface modified plasma sprayed alumina coatings, Surf. Eng. 18 (2002) 208–212, https://doi.org/10.1179/026708402225005241.
[27] R. Krishnan, S. Dash, R. Kesavamoorthy, C. Babu Rao, A.K. Tyagi, B. Raj, Laser surface modification and characterization of air plasma sprayed alumina coatings, Surf. Coatings Technol. 200 (2006) 2791–2799, https://doi.org/10.1016/j.surfcoat.2005.05.002.
[28] F.E. de Freitas, F.P. Briguente, Reis A.G.D, G. de Vasconcelos, D.A.P. Reis, Investigation on the microstructure and creep behavior of laser remelted thermal barrier coating, Surf. Coatings Technol. 369 (2019) 257–264, https://doi.org/10.1016/j.surfcoat.2019.04.068.
[29] N.K. Tolochko, T. Laoui, Y.V. Khlopkov, S.E. Mozzharov, V.I. Titov, M.B. Ignatiev, Absortance of powder materials suitable for laser sintering, Rapid Prototyp. J. 6 (2000) 155–161, https://doi.org/10.1108/13552540010337029.
[30] R.S. Pavlov, J. Guimbao, F. Ramos, Low-power laser-induced absorption in YSZ ceramics through formation of F-centers, Opt. Laser. Technol. 121 (2000), 105759, https://doi.org/10.1016/j.optlastec.2019.105759.
[31] B. Qian, Z. Shen, Laser sintering of ceramics, J. Asian Ceram. Soc. 1 (2013) 315–321, https://doi.org/10.1016/j.jascer.2013.08.004.
[32] A.N. Samant, N.B. Dahotre, Laser machining of structural ceramics – A review, J. Eur. Ceram. Soc. 29 (2009) 969–993, https://doi.org/10.1016/j.jeurceramsoc.2008.11.010.
[33] Z. Fan, M. Lu, H. Huang, Selective laser melting of alumina: a single track study, Ceram. Intern. 44 (2018) 9484–9493, https://doi.org/10.1016/j.ceramint.2018.02.166.
[34] Y. Zheng, K. Zhang, T.T. Liu, W.H. Liao, C.D. Zhang, H. Shao, Cracks of alumina ceramics by selective laser melting, Ceram. Int. 45 (2019) 175–184, https://doi.org/10.1016/j.ceramint.2018.09.149.
[35] S. Das, A.K. Nath, P.P. Bandyopadhyay, Online monitoring of laser remelting of plasma sprayed coatings to study the effect of cooling rate on residual stress and mechanical properties, Ceram. Int. 44 (2018) 7524–7534, https://doi.org/10.1016/j.ceramint.2018.01.152.
[36] B.S. Yilbas, S.S. Akhtar, C. Karatas, Laser Cutting of alumina tiles: heating and stress analysis, J. Manuf. Process. 15 (2013) 14–24, https://doi.org/10.1016/j.jmapro.2012.08.001.
[37] Y.-.C. Hagedorn, J. Wilkes, W. Wilhelm, K. Wissenbach, R. Poprawe, Net shaped high performance oxide ceramic parts by selective laser melting, Phys. Procedia 5 (2010) 587–594, https://doi.org/10.1016/j.phpro.2010.08.086.
[38] F. Rey-García, F. Gutiérrez-Mora, C.J. Borrell. L.C. Estepa, L.A. Angurel, G.F. de la Fuente, Microstructural characterization and tribological behavior of Laser Furnace processed ceramic tiles, Ceram. Int. 44 (2018) 6997–7005, https://doi.org/10.1016/j.ceramint.2018.01.133.
[39] I.G. Cano, D. Dosta, J.R. Miguel, J.M. Guilemany, Production and characterization of metastable Al_2O_3–TiO_2 ceramic materials, J. Mater. Sci. 42 (2007) 9331–9335, https://doi.org/10.1007/s10853-007-1871-8.
[40] S. Dosta, M. Torrell, I.G. Cano, J.M. Guilemany, Functional colored ceramic coatings obtained by thermal spray for decorative applications, J. Eur. Ceram. Soc. 32 (2012) 3685–3692, https://doi.org/10.1016/j.jeurceramsoc.2012.04.026.
[41] D. Rodriguez, I.G. Cano, J. Fernandez, J.C. Fariñas, R. Moreno, Rheological behaviour of submicron mullite carbon nanofiber suspensions for Atmospheric Plasma Spraying coatings, J. Eur. Ceram. Soc. 34 (2014) 475–483, https://doi.org/10.1016/j.jeurceramsoc.2013.07.019.
[42] Y. Xian, P. Zhang, S. Zhai, P. Yuan, D. Yang, Experimental characterization methods for thermal contact resistance: a review, Appl. Therm. Eng. 130 (2018) 1530–1548, https://doi.org/10.1016/j.applthermaleng.2017.10.163.
[43] R. McPherson, Formation of metastable phases in flame- and plasma-prepared alumina, J. Mater. Sci. 8 (1973) 851–858, https://doi.org/10.1007/BF02397914.

[44] J. Suffner, M. Latteman, H. Hahn, L. Giebeler, C. Hess, I.G. Cano, S. Dosta, J. M. Guilemany, C. Musa, A.M. Locci, R. Licheri, R. Orrú, G. Cao, Microstructure evolution during spark plasma sintering of metastable (ZrO_2–3 mol% Y_2O_3)–20 wt % Al_2O_3 composite powders, J. Am. Ceram. Soc. 93 (2010) 2864–2870, https://doi.org/10.1111/j.1551-2916.2010.03752.x.

[45] J. Suffner, H. Sieger, H. Hahn. S. Dosta, I.G. Cano, J.M. Guilemany, P. Klimczyk, L. Jaworska, Microstructure and mechanical properties of near-eutectic ZrO_2–60 wt.% Al_2O_3 produced by quenched plasma spraying, Mater. Sci. Eng. A 506 (2009) 180–186, https://doi.org/10.1016/j.msea.2008.11.034.

[46] M. Plummer, The formation of metastable aluminas at high temperatures, J. Appl. Chem. 8 (1958) 35–44, https://doi.org/10.1002/jctb.5010080107.

[47] Pressure measuring film, Prescale, instruction manual. Available on line, https://www.fujifilm.eu/fileadmin/products/prescale/media/Mono_Sheet_Type_for_Medium_Pressure_klein.pdf.